ACS NANO

www.acsnano.org

ARTICLE

High Responsivity, Large-Area Graphene/MoS_2 Flexible Photodetectors

Domenico De Fazio,[†,§] Ilya Goykhman,[†,§] Duhee Yoon,[†] Matteo Bruna,[†] Anna Eiden,[†] Silvia Milana,[†] Ugo Sassi,[†] Matteo Barbone,[†] Dumitru Dumcenco,[‡] Kolyo Marinov,[‡] Andras Kis,[‡] and Andrea C. Ferrari*[,†]

[†]Cambridge Graphene Centre, University of Cambridge, Cambridge CB3 0FA, United Kingdom

[‡]Electrical Engineering Institute, Ecole Polytechnique Federale de Lausanne, Lausanne CH-1015, Switzerland

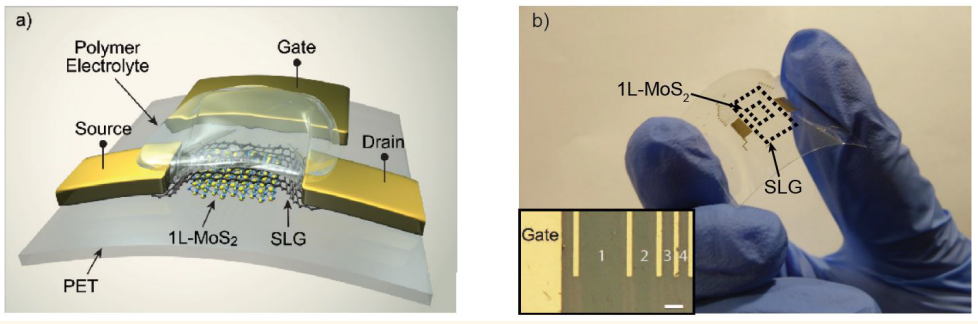

ABSTRACT: **We present flexible photodetectors (PDs) for visible wavelengths fabricated by stacking centimeter-scale chemical vapor deposited (CVD) single layer graphene (SLG) and single layer CVD MoS_2, both wet transferred onto a flexible polyethylene terephthalate substrate. The operation mechanism relies on injection of photoexcited electrons from MoS_2 to the SLG channel. The external responsivity is 45.5A/W and the internal 570A/W at 642 nm. This is at least 2 orders of magnitude higher than bulk-semiconductor flexible membranes. The photoconductive gain is up to 4×10^5. The photocurrent is in the 0.1−100 μA range. The devices are semitransparent, with 8% absorptance at 642 nm, and are stable upon bending to a curvature of 1.4 cm. These capabilities and the low-voltage operation (<1 V) make them attractive for wearable applications.**

KEYWORDS: *photodetectors, graphene, MoS_2, heterostructures, flexible optoelectronics*

Modern electronic and optoelectronic systems, such as smart phones, smart glasses, smart watches, wearable devices, and electronic tattoos, increasingly require ultrathin, transparent, low-cost, and energy efficient devices on flexible substrates.[1] The rising demand for flexible electronics and optoelectronics requires materials that can provide a variety of electrical and optical functionalities, with constant performance upon application of strain.[2] A wide range of optoelectronic devices on flexible substrates have been reported to date, such as photodetectors (PDs),[3,4] light emitting diodes (LEDs),[5] optical filters,[6] optical interconnects,[7,8] photovoltaic devices,[9,10] and biomedical sensors.[11,12]

Major challenges in the development of flexible optoelectronic devices stem from the limitations associated with the high stiffness of bulk semiconductors.[13,14] In the case of flexible PDs, the current approaches primarily rely on thin (μm-thick) semiconductor membranes[4,15] and compound semiconductor nanowires (NWs),[3,16−18] mainly because of their ability to absorb light throughout the whole visible range (0.4−0.7 μm) and the possibility to adapt their fabrication techniques from rigid to plastic, or deformable substrates.[1]

One of the key parameters for PDs characterization is the responsivity. This is defined as the ratio between the collected photocurrent (I_{ph}) and the optical power. The responsivity is named external ($R_{ext} = I_{ph}/P_o$)[19] or internal ($R_{int} = I_{ph}/P_{abs}$),[19] whenever the incident (P_o) or absorbed (P_{abs}) optical power is used in the denominator. Since not all incident photons are absorbed by a PD, *i.e.*, $P_{abs} < P_o$, then R_{int} is typically larger than R_{ext}.[19]

In flexible PDs, R_{ext} up to~ 0.3 A/W was reported for crystalline semiconductor membranes (InP, Ge)[4,15] with integrated p−i−n junctions, showing photocurrent up to~ 100 μA, with~ 30% degradation upon bending at a radius $r_b \sim$ 3 cm.[15] PDs made of a single semiconductor NW on flexible substrates[3,16−18] demonstrated R_{ext} up to~ 10^5 A/W, for r_b down to 0.3 cm.[3] Yet, these provide limited I_{ph} in the order of nA[3,16,18] up to <1 μA.[17] For flexible devices exploiting NW arrays by drop-casting,[3,16,18] rather than based on single NWs,

Received: July 30, 2016
Accepted: August 18, 2016
Published: August 18, 2016

DOI: 10.1021/acsnano.6b05109
ACS Nano 2016, 10, 8252−8262

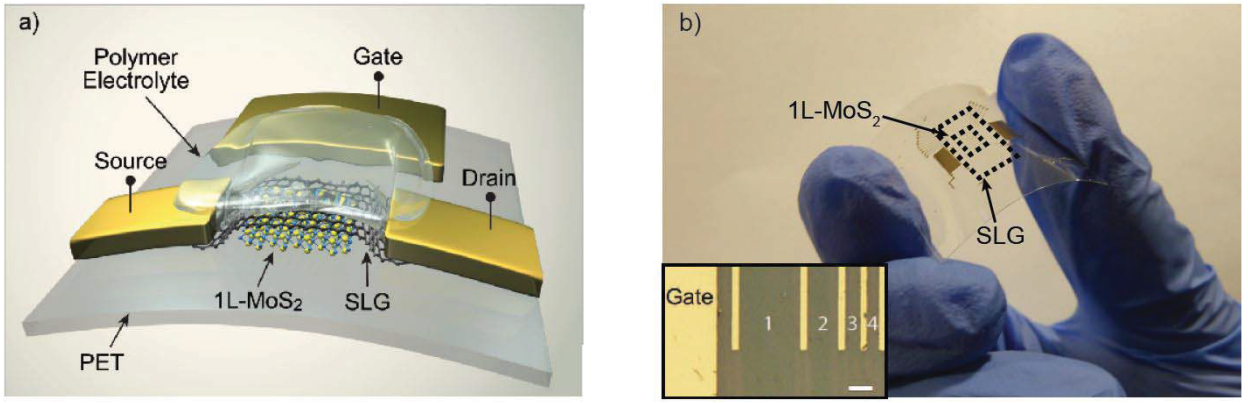

Figure 1. (a) Schematic SLG/MoS_2 flexible PD, side-gated with a PE. (b) Picture of a typical PD, showing transparency and flexibility. (Inset) Optical image of 4 PDs with different channel lengths and common side gate electrode. Scale bar is 200 μm.

R_{ext} degrades significantly from ~10^5 A/W to the mA/W range,[3,16,18] due to photocurrent loss at multiple junctions in the NW network.[3,16,18]

Graphene and related materials (GRMs) have great potential in photonics and optoelectronics.[20−23] A variety of GRM-based devices have been reported, such as flexible displays,[24] photovoltaic modules,[25,26] photodetectors,[22,27−29] optical modulators,[30] plasmonic devices,[31−35] and ultrafast lasers.[23] Heterostructures, obtained by stacking layers of different materials, were also explored,[21,22] *e.g.*, in photovoltaic[36] and light emitting devices.[37]

Flexible PDs based on GRMs were studied for ultraviolet,[38,39] visible,[40−45] and near-infrared bands.[46,47] In these devices, different materials and heterostructures produced by mechanical exfoliation,[40,41] Chemical Vapor Deposition (CVD),[42,43,46] and liquid-phase exfoliation (LPE)[44,45,47] were employed. The flexible PDs produced by mechanical exfoliation[40,41] have a small (~μm^2) photoactive area, and they cannot be scaled up to mass production. LPE-based PDs have low (<mA/W)[44,45] responsivity. Ref 47 showed that thick (~μm) films of chemically modified, charge-transfer optimized, LPE-produced, $MoSe_2$ and MoS_2 polymer composites can provide ~ A/W responsivity[47] at near-infrared bands. Nevertheless, these PDs require high (~10 V) operation voltage and are nontransparent. Flexible PDs at 450 nm using CVD MoS_2 transistors[42] and MoS_2/WS_2 heterostructures[43] were previously reported, and PDs at 780 nm were prepared from doped SLG p−n junctions.[38] However, these devices have responsivity in the mA/W range. CVD-based SLG/MoS_2 heterostructures[48] showed good photodetection on rigid Si/SiO_2 substrates, with back-gate-dependent R_{int} ~ 10^8A/W for optical intensities <0.1pW/μm^2.

Here we demonstrate a polymer electrolyte (PE) gated, CVD-based, flexible PD, for visible wavelengths, with large (~mm^2) photoactive area combined with high responsivity (~hundreds A/W), high (>80%) transparency, gate tunability, low (<1 V) operation voltage, and stable (±12%) I_{ph} upon multiple (>30) bending cycles. The device is assembled by stacking on a PET substrate a centimeter-scale CVD single layer graphene (SLG) on top of a CVD-grown single layer MoS_2 (1L-MoS_2). In this configuration, 1L-MoS_2 acts as visible light absorber, while SLG is the conductive channel for photocurrent flow.[48] We show that R_{ext} can be increased by promoting carrier injection from 1L-MoS_2 to SLG using PE gating, or by increasing the source-drain voltage. This is achieved in devices with~ 82% transparency, twice that reported for semiconductor membrane devices.[15] We get R_{int} ~ 570A/W for ~0.1nW/μm^2 at 642 nm, similar to SLG/MoS_2 PDs[48] on rigid substrates operating at the same optical power. This shows that SLG/MoS_2 heterostructures on PET retain their photodetection capabilities. We note that the devices from ref 48 have at least 2 orders of magnitude smaller photoactive area with respect to ours, and they are not flexible, not transparent, and require tens of volts operation, unlike the <1 V of ours. Upon bending, our PDs have stable performance for r_b down to ~1.4 cm. This is comparable to r_b measured in semiconductor membranes PDs,[4,15] which show lower (<0.3 A/W) responsivities.[4,15] Although our r_b is 1 order of magnitude larger than for flexible single NWs,[3,16−18] the latter had at least 3 orders of magnitude smaller device areas (<5 μm^2)[3,16−18] compared to our PDs (>0.2 mm^2). Given the responsivity, flexibility, transparency, and low operation voltage, our PDs may be integrated in wearable, biomedical, and low-power optoelectronic applications.[11,12,17]

RESULTS

Figure 1a plots a schematic drawing of our PDs. We fabricated 4 PD arrays with 10 devices each, with channel lengths of 100 μm, 200 μm, 500 μm, and 1 mm. Each device consists of a 1L-MoS_2 absorber covered by a SLG channel, clamped between source and drain electrodes. We chose PET as a flexible substrate due to its ~90% transparency in the visible range[49] and ability to withstand solvents (*e.g.*, acetone and isopropyl alcohol)[50] commonly used in the transfer processes of layered materials grown by CVD (*e.g.*, transfer of SLG grown on Cu).[51] A 1L-MoS_2 is used as absorber in order to preserve >80% transparency, considered suitable by industry for wearable applications,[52] Figure 1b. The SLG/1L-MoS_2 heterostructure is gated using a PE.[53,54]

The operation principle of our devices is depicted in Figure 2. For energy bands alignment, the electron affinity of 1L-MoS_2 and the Dirac point of SLG are assumed to be ~4−4.2 eV[55,56] and ~4.6 eV,[57,58] respectively. We also assume SLG to be initially p-doped (Figure 2a), as reported in previous works involving SLG transferred on PET.[59,60] At zero voltage the device is in thermodynamic equilibrium with a constant Fermi level (E_F) and zero current flow between the layers. During illumination and photon absorption in MoS_2, part of the photogenerated electrons would be injected from the 1L-MoS_2 conduction band into the lower energy states in p-doped

DOI: 10.1021/acsnano.6b05109
ACS Nano 2016, 10, 8252−8262

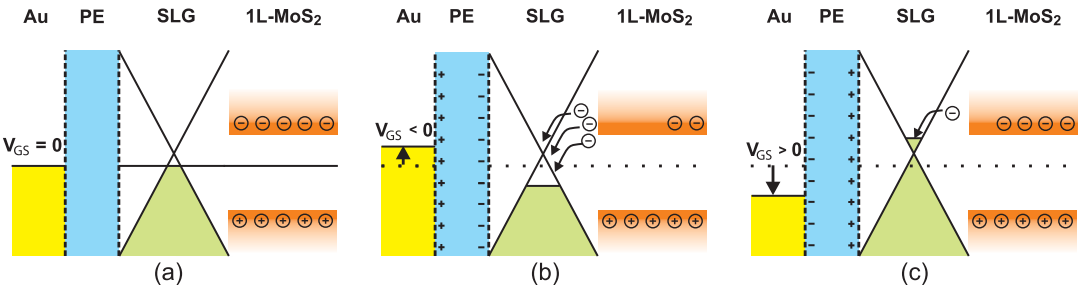

Figure 2. Schematic band diagram of PE gated SLG/1L-MoS_2 PD at (a) zero, (b) negative, and (c) positive V_{GS}.

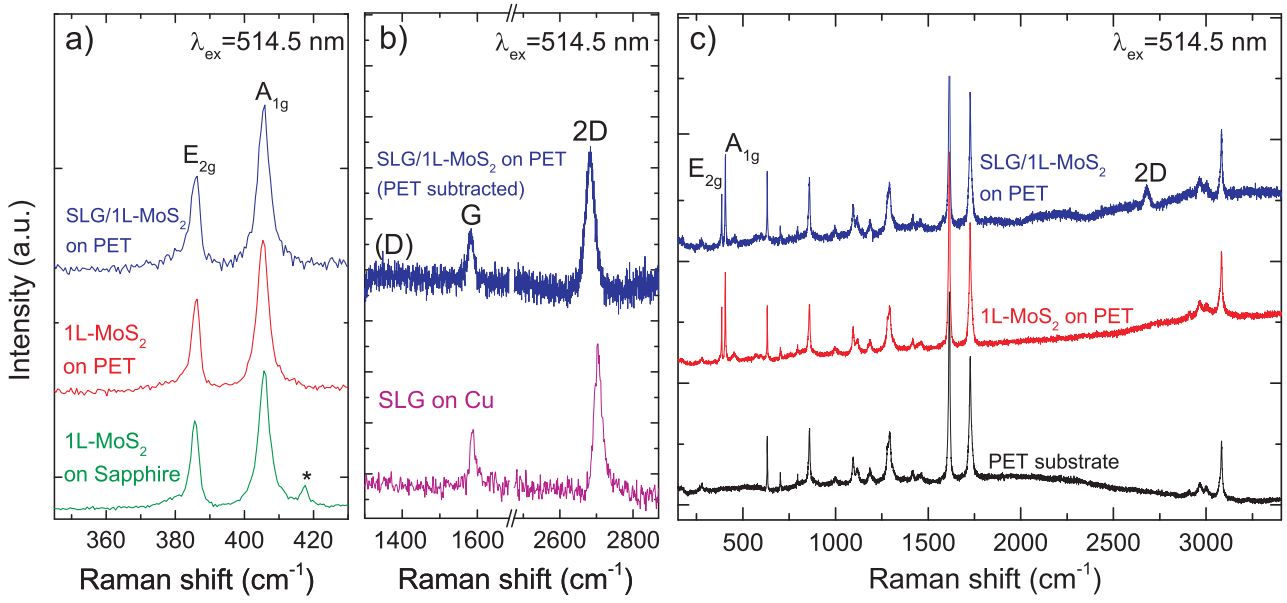

Figure 3. (a) Raman spectra at 514 nm for 1L-MoS_2 on sapphire, 1L-MoS_2 on PET, and SLG/1L-MoS_2. (b) Comparison at 514 nm of the Raman spectra of as-grown SLG on Cu (magenta curve) and SLG/1L-MoS_2 after transfer on PET and normalized subtraction of the PET substrate signal (blue curve). (c) Raman spectra at 514 nm of PET substrate (black curve), 1L-MoS_2 on PET (red curve) and SLG/1L-MoS_2 on PET (blue curve).

SLG,[48] leaving behind the uncompensated charge of photogenerated holes. The latter would be trapped in 1L-MoS_2 and act as an additional positive gate voltage, V_{GS}, applied to the SLG channel, resulting in a shift of the charge neutrality point (V_{CNP}) to more negative voltages. The injected electrons from 1L-MoS_2 would occupy energy states above E_F (Figure 2b), thus reducing the hole concentration and decreasing the hole current in the SLG channel. Electron injection can be further promoted by gating. When a negative V_{GS} is applied, higher p-doping of the SLG channel would induce a stronger electric field at the SLG/1L-MoS_2 interface,[48] thus favoring electron transfer from 1L-MoS_2 (Figure 2b). Hence, for negative V_{GS}, R_{ext} is expected to increase, due to injection of more photoelectrons to SLG and consequent more pronounced current reduction. The opposite should happen for positive V_{GS}, where the gate-induced negative charge in SLG would reduce the p-doping and shift E_F toward the Dirac point. In this case, the photogenerated electrons in 1L-MoS_2 would experience weaker electric fields at the SLG/1L-MoS_2 interface[48] and would become less attracted by the SLG channel. Thus, we expect R_{ext} to decrease. For high enough positive V_{GS}, E_F would cross the Dirac point, and SLG becomes n-doped (Figure 2c). As a result, only a weak electron injection from 1L-MoS_2 would be possible, if E_F in SLG remains below the 1L-MoS_2 conduction band, retaining a weak electric field at the interface. In this regime, the transferred electrons would increase the free carrier concentration in the n-doped channel, hence only minor increments of R_{ext} and I_{ph} are expected.

Our devices are built as follows: 1L-MoS_2 is epitaxially grown by CVD on c-plane sapphire substrates,[61] while SLG is grown on a 35 μm Cu foil, following the process described in refs 51 and 62 (see Methods for details). Prior to assembling the SLG/MoS_2 stack, the quality and uniformity of MoS_2 on sapphire and SLG on Cu are inspected by Raman spectroscopy and photoluminescence (PL), using a Horiba Jobin Yvon HR800 spectrometer equipped with a 100× objective. The laser power is kept below 100 μW (spot size <1 μm) to avoid possible heating effects or damage. Figure 3a (green curve) plots the Raman spectrum of CVD MoS_2 on sapphire for 514 nm excitation. The peak at ~385 cm^{-1} corresponds to the in-plane (E^1_{2g}) mode,[63,64] while that at ~404 cm^{-1} is the out of plane (A_{1g}) mode,[63,64] with full width at half-maximum FWHM (E^1_{2g}) = 2.5 and FWHM(A_{1g}) = 3.6 cm^{-1}, respectively. The E^1_{2g} mode softens, whereas the A_{1g} stiffens with increasing layer thickness,[65,66] so that their frequency difference can be used to monitor the number of layers.[65] The peak position difference ~20 cm^{-1} is an indicator of 1L-MoS_2.[65] The peak at~ 417 cm^{-1} (marked by an asterisk in Figure 3a) corresponds to the A_{1g} mode of sapphire.[67]

DOI: 10.1021/acsnano.6b05109
ACS Nano 2016, 10, 8252–8262

The Raman spectrum measured at 514 nm of SLG on Cu is shown in Figure 3b (magenta curve). This is obtained after the removal of the background PL of Cu.[68] The two most intense features are the G and the 2D peak, with no significant D peak. The G peak corresponds to the E_{2g} phonon at the Brillouin zone center.[69] The D peak is due to the breathing modes of sp^2 rings and requires a defect for its activation by double resonance.[69−72] The 2D peak is the second order of the D peak.[69] This is always seen, even when no D peak is present, since no defects are required for the activation of two phonons with the same momentum, one backscattering from the other.[69] In our sample, the 2D peak is a single sharp Lorentzian with FWHM(2D) ∼26 cm^{-1}, a signature of SLG.[70] Different (∼20) measurements show similar spectra, indicating uniform quality throughout the sample. The position of the G peak, Pos(G), is ∼1588 cm^{-1}, with FWHM(G) ∼6 cm^{-1}. The 2D peak position, Pos(2D) is ∼2705 cm^{-1}, while the 2D to G peak intensity and area ratios, I(2D)/I(G) and A(2D)/A(G), are ∼2.6 and ∼5.8, respectively, indicating a p-doping ∼300 meV,[53,73,74] which corresponds to a carrier concentration $\sim 6 \times 10^{12} cm^{-2}$.

Another evidence for 1L-MoS_2 comes from the PL spectrum [Figure 4a (green curve)], showing a peak at ∼658 nm (∼1.88 eV), due to band-to-band radiative recombination in 1L-MoS_2.[75]

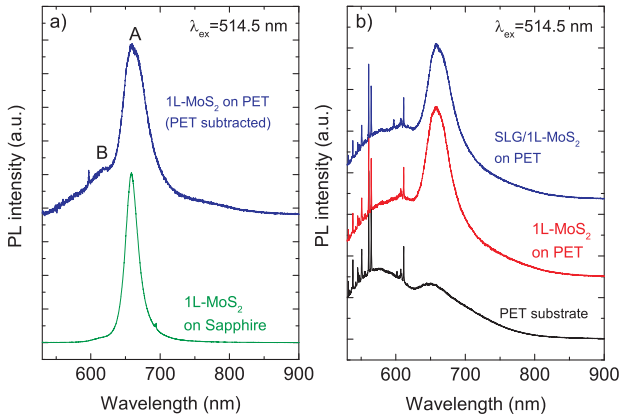

Figure 4. (a) PL spectrum at 514 nm (2.41 eV) of 1L-MoS_2 on sapphire and 1L-MoS_2 after transfer on PET. (b) PL spectra of PET substrate (black curve), 1L-MoS_2 on PET (red curve), and SLG/1L-MoS_2 on PET (blue curve).

Then, the MoS_2 film is transferred onto a PET substrate from sapphire using a KOH-based approach.[61] The samples are first spin coated with ∼100 nm poly(methyl methacrylate) (PMMA). This is detached in a 30% KOH solution, washed in deionized (DI) water, and transferred onto PET. The PMMA is then dissolved in acetone. Subsequently, SLG is transferred on the 1L-MoS_2 on PET. PMMA is spin coated on the SLG/Cu substrate and then placed in a solution of ammonium persulfate (APS) in DI water until Cu is etched.[51,76] The PMMA membrane with attached SLG is then transferred to a beaker filled with DI water for cleaning APS residuals. The membrane is subsequently lifted with the target PET substrate, having 1L-MoS_2 on top. After drying, PMMA is removed in acetone leaving SLG on 1L-MoS_2.

Raman and PL characterizations are performed at each step of the SLG/1L-MoS_2 assembly on PET, *i.e.*, on 1L-MoS_2 transferred on PET and on SLG on 1L-MoS_2. This is to confirm no degradation during the fabrication process. Figure 3a (red curve) plots the Raman spectrum of 1L-MoS_2 on PET. The frequency difference between E^1_{2g} and A_{1g} and the FWHMs are preserved on PET, suggesting no degradation. The PL spectrum of 1L-MoS_2 on PET is shown in Figure 4b (red curve). The signal from 1L-MoS_2 is convolved within the background due to the PET substrate [Figure 4b (black curve)]. In order to reveal the underlying PL signature of 1L-MoS_2, we use a point-to-point subtraction between the spectrum of 1L-MoS_2 on PET [Figure 4b (red curve)] and the reference PET spectrum [Figure 4b (black curve)]. Prior to subtraction, the spectra are normalized to the intensity of the Raman peak at ∼1615 cm^{-1} (corresponding to the peak at ∼560 nm in Figure 4b), due to the stretching vibrations of benzene rings in PET.[77] As a result, the PL signal of 1L-MoS_2 can be seen in Figure 4a (blue curve) revealing no significant changes after transfer. The subsequent transfer of SLG on 1L-MoS_2 does not alter the 1L-MoS_2 PL position and line shape [Figure 4b (blue curve)].

We then characterize the SLG transferred on 1L-MoS_2/PET. The intense Raman features of the underlying PET substrate[77] [Figure 3c (black curve)] mask the SLG peaks. In order to reveal the Raman signatures of SLG, we first measure the reference spectrum, shown in Figure 3c (black curve), of a PET substrate, using identical conditions as those for SLG/1L-MoS_2/PET. We then implement a point-to-point subtraction, normalized to the intensity of the PET peak at ∼1615 cm^{-1}, of the PET reference spectrum, Figure 3c (black curve), from the total spectrum, Figure 3c (blue curve). The result is in Figure

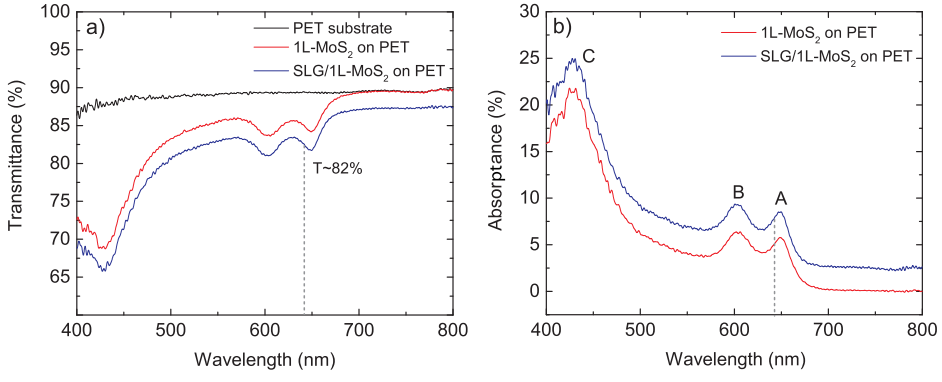

Figure 5. (a) Transmittance of PET (black curve), 1L-MoS_2 on PET (red curve), and SLG/1L-MoS_2 on PET (blue curve). (b) Absorptance of 1L-MoS_2 and SLG/1L-MoS_2 as derived from the transmittance measurements. Dashed lines indicate our test wavelength.

DOI: 10.1021/acsnano.6b05109
ACS Nano 2016, 10, 8252−8262

3b (blue curve). The 2D peak retains its single-Lorentzian lineshape with FWHM(2D) ~28 cm^{-1}, validating the transfer of SLG. The negligible D peak indicates that no significant defects are induced during transfer. Pos(G) is ~1583 cm^{-1}, FWHM(G) ~ 17 cm^{-1}, Pos(2D) ~ 2683 cm^{-1}, and A(2D)/A(G) ~ 4.8, indicating a p-doping ~4 × $10^{12}cm^{-2}$ (~250 meV).[53,73]

We then measure the absorptance and transmittance of SLG/1L-MoS_2 using a broadband (400−1300 nm) white light from a tungsten halogen lamp. The transmitted light is collected by a 10× objective lens (NA = 0.25) with a Horiba Jobin Yvon HR800 spectrometer equipped with a 300 grooves/mm grating, charged coupled device (CCD) detector and a 50 μm pinhole. Figure 5a plots the optical transmittance of bare PET (T_{PET}, black line), 1L-MoS_2 on PET (T_{MoS_2}, red line), and the final SLG/1L-MoS_2 stack on PET (T_{Hetero}, blue line) measured in the 400−800 nm wavelength range. Figure 5b plots the absorptance of 1L-MoS_2 on PET (Abs_{MoS_2}, red line) and of SLG/1L-MoS_2 on PET (Abs_{Hetero}, blue line), calculated as $Abs_{MoS_2} = (T_{PET} - T_{MoS_2})/T_{PET}$ and $Abs_{Hetero} = (T_{PET} - T_{Hetero})/T_{PET}$. The three peaks in Figure 5b at ~650 nm (1.91 eV), ~603 nm (2.06 eV), and ~428 nm (2.90 eV) correspond to the A, B, C excitons of 1L-MoS_2.[75,78] Their positions remain unchanged after SLG transfer. The absorptance difference between the two curves (red and blue) is ~2.6%, consistent with the additional SLG absorption.[79]

The PD area is shaped by etching, whereby SLG extending beyond the 1L-MoS_2 flake is removed in an oxygen plasma. The source, drain and gate electrodes are then defined by patterning the contacts area, followed by Cr/Au (6 nm/60 nm) evaporation and lift-off. PDs with different channels lengths (100 μm to 1 mm), 2 mm channel width, and common side-gate electrodes (1 × 0.5 cm) are built (Figure 1b).

Ref 48 showed that the responsivity of SLG/MoS_2 PDs can be enhanced by gating. This induces a stronger electric field at the SLG/MoS_2 interface and promotes charge transfer. Various gating techniques have been exploited for GRM-based devices, including conventional Si/SiO_2 back-gates,[80] high-k dielectrics (Al_2O_3, HfO_2),[81] chemical dopants,[82] ionic liquids,[83] and PEs.[53,74] In order to gate our SLG/1L-MoS_2 on PET, we employ the latter due to its compatibility with flexible substrates[84] and the ability to substantially dope SLG (±0.8 eV)[53,74] using small gate voltages (up to 4 V), unlike other gating techniques, which would require considerably higher biases to reach the same doping.[80,82] We use a PE consisting of $LiClO_4$ and poly(ethylene oxide) (POE).[53,74] We place the PE over both the SLG channel and the side-gate electrode. To evaluate the effect of PE deposition on the SLG channel doping, we use Raman analysis. We get Pos(G) ~ 1583 cm^{-1}, FWHM(G) ~ 19 cm^{-1}, Pos(2D) ~ 2686 cm^{-1}, and A(2D)/A(G) ~ 5.3, consistent with a small reduction of p-doping to ~230 meV.[53,73] For electrical measurements we apply −1 V < V_{GS} < 1 V in order to avoid electrochemical reactions, such as hydrolysis of residual water in the electrolyte.[85,86] These may permanently modify the graphene electrode[85,86] and compromise the stability and performance of the device. To control the stability of the PE gating, we continuously monitor the gate leakage current (I_{gate}), keeping I_{gate} < 1 nA throughout the experiments. The devices are tested ~30 times, showing no degradation in the leakage current over at least six months.

We then characterize the responsivity at 642 nm (~1.93 eV), slightly above the A exciton peak, where absorption of 1L-MoS_2 is maximized (Figure 5b). At 642 nm the SLG/1L-MoS_2 heterostructure shows ~8% absorptance (Figure 5b), and the device retains ~82% transparency (Figure 5a).

The I_{DS}−V_{GS} measurements in Figure 6a are done at room temperature using a probe station and a parameter analyzer

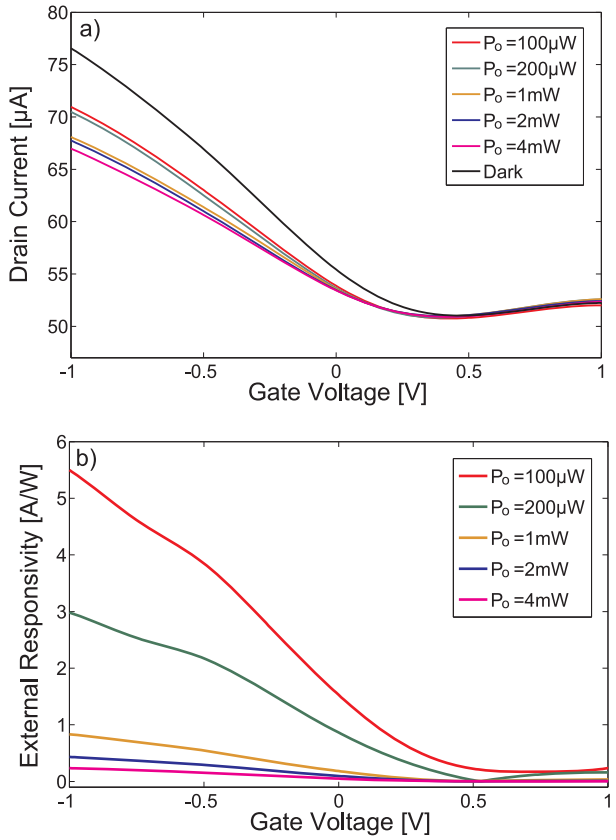

Figure 6. (a) Transfer characteristics as a function of P_o. (b) R_{ext} as a function of V_{GS} and P_o. Channel length and width are 100 μm and 2 mm, respectively.

(Keithley 4200). The PD is illuminated at normal incidence by a collimated laser with P_o ranging from 100 μW to 4 mW. At these P_o and with V_{DS} = 0.1 V we measure a positive V_{CNP} ranging from ~0.39 to 0.47 V, indicating an initial SLG p-doping ~220 meV, consistent with the Raman estimate.

Figure 6a shows that for −1 V < V_{GS} < 0.5 V, where SLG transport is hole dominated, the current decreases under illumination (~10 μA at V_{GS} = −1 V), as anticipated from the band-diagram of Figure 2. For V_{GS} > 0.5 V, where SLG is electron-doped, the PD shows a small (up to ~0.2μA) current increase under illumination. Figure 6b plots R_{ext} as a function of V_{GS}, as derived from transconductance measurements using:[19]

$$R_{ext} = \frac{|I_{light} - I_{dark}|}{P_o \cdot A_{PD}/A_o} \quad (1)$$

where I_{light} and I_{dark} are the PD current under illumination and in dark, $|I_{light} - I_{dark}| = I_{ph}$ is the photocurrent defined as the absolute change in the device current upon illumination, A_o is the laser spot area, A_{PD} is the PD area, and A_{PD}/A_o is a scaling factor that takes into account the fact that only a fraction of optical power impinges on the PD. As expected from the band-diagram in Figure 2, R_{ext} tends to increase for more negative V_{GS}, up to ~5.5 A/W at V_{GS} = −1 V, V_{DS} = 0.1 V for P_o = 100 μW. By taking into account that only 8% of light is absorbed

DOI: 10.1021/acsnano.6b05109
ACS Nano 2016, 10, 8252−8262

(P_{abs} = 0.08 × P_o), we derive R_{int} = R_{ext}/0.08 = 69A/W. Figure 6b implies that the higher P_o, the lower R_{ext}. This can be explained considering that the more photogenerated electrons are injected into the p-doped channel, the lower the electric field at the SLG/1L-MoS_2 interface, therefore a reduced injection of electrons causes R_{ext} to decrease.

Given that R_{ext},R_{int} > 1A/W, we expect a photoconductive gain (G_{PD}),[19,87] whereby absorption of one photon results in multiple charge carriers contributing to I_{ph}. Our PDs act as optically gated photoconductors, where the SLG conductance is modulated by optical absorption in the 1L-MoS_2. In this configuration, the presence of G_{PD} implies that the injected electrons in SLG can recirculate multiple times between source and drain, before recombining with trapped holes in 1L-MoS_2. Consequently, G_{PD} can be estimated as the ratio of electrons recombination (τ_{rec}) and transit (t_{tr}) times in the SLG channel: G_{PD} = τ_{rec}/t_{tr}.[19,21,22,87] For higher V_{DS}, the free carriers drift velocity υ_d in the SLG channel increases linearly with bias (ohmic region) until it saturates, because of carriers scattering with optical phonons.[88] The linear increase in υ_d results in shorter t_{tr}, with t_{tr} = L/υ_d, where L is the channel length.[19,21,22,87] Therefore, G_{PD} is also expected to grow linearly with V_{DS}, providing higher R_{ext}. To confirm the photoconductive nature of G_{PD} in our devices and test the dependence of R_{ext} on V_{DS}, we measure I_{DS}−V_{DS} under illumination at P_o = 100 μW for V_{GS} = −1 V and calculate R_{ext} using eq 1. The I_{DS}−V_{DS} characteristics of the PD show linear dependence, confirming ohmic behavior of the metal-SLG-metal channel.[89] We use V_{DS} < 1 V to keep the device operation in the linear (ohmic) regime and minimize the effects of the nonlinear dependence of υ_d on V_{DS} (such as velocity saturation) that might appear for V_{DS} > 1 V.[88] As shown in Figure 7, R_{ext} scales with V_{DS} and reaches ∼45.5A/W (R_{int} ∼ 570A/W) at V_{DS} = 1 V. This is almost 1 order of magnitude higher than at V_{DS} = 0.1 V, consistent with the similar increase in V_{DS}. These results are at least 2 orders of magnitude higher than semiconductor flexible membranes.[4,15] Furthermore, such a combination of high responsivity with μA range photocurrent surpasses that found in other GRM-based PDs in the visible range.[40−45,47] We also fabricate a control device with a 1L-MoS_2 channel only, without SLG. This has R_{ext} ∼ 2 mA/W, which is 4 orders of magnitude smaller than that of our SLG/1L-MoS_2 heterostructure. We thus conclude that SLG/1L-MoS_2 heterostructures are necessary to achieve high (hundreds A/W) responsivity, due to the presence of photoconductive gain.

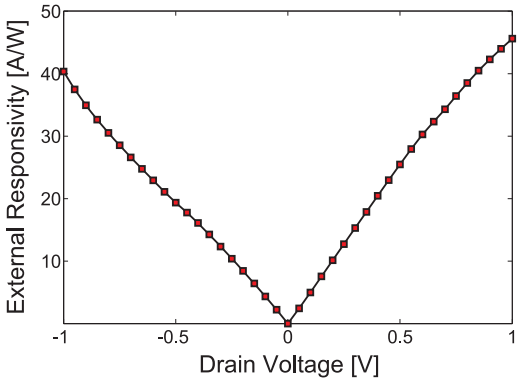

Figure 7. R_{ext} as a function of V_{DS} for P_o = 100 μW at V_{GS} = −1 V.

To assess the photoresponse uniformity in our SLG/1L-MoS_2 heterostructures, we perform photocurrent mapping using the same laser source (642 nm) as for optoelectronic characterizations. We scan areas of 80 × 140 μm (pixel size 3 × 3 μm) at different locations. At each position (pixel) the device photocurrent is measured for V_{DS} = 0.3 V (Figure 8a). We also collect the backscattered light to give a reflection map (Figure 8b). Figure 8a indicates that the entire channel area confined between the source-drain electrodes is photoactive, and shows uniform photocurrent photoresponse with standard deviation ±15%. We thus conclude that interface imperfections (*e.g.*, bubbles, polymer residuals, *etc.*) have minor effect on the charge transfer process from MoS_2 to graphene.

We define G_{PD} as the ratio between electrons recirculating in the SLG channel, thus sustaining I_{ph}, and the initial electron concentration injected into SLG from 1L-MoS_2:[48]

$$G_{PD} = \frac{|I_{light} - I_{dark}|}{q \cdot A_{PD} \cdot \Delta n_{ch}} \quad (2)$$

where q is the electron charge and Δn_{ch} is the concentration per unit area and per unit time of the injected electrons. Δn_{ch} is equal to the trapped-hole concentration per unit area and per unit time in 1L-MoS_2, which is related to a charge neutrality point shift ΔV_{GS} = ΔV_{CNP} in the transfer characteristics. To calculate Δn_{ch}, we first write the potential balance in the metal-dielectric-SLG structure. When V_{GS} is applied, it creates a gate-to-channel potential drop (V_{diel}), and it induces a local electrostatic potential in the graphene channel (V_{ch} = E_F/q):[19,53]

$$V_{GS} = V_{diel} + V_{ch} = \frac{Q_G}{C_G} + V_{ch} \quad (3)$$

where Q_G and C_G are the charge concentration and the geometrical capacitance per unit area associated with the gate electrode, respectively. $|Q_G|$ = $|q \cdot n_{ch}|$, reflecting the charge neutrality of the gate capacitor, with n_{ch} the charge carrier concentration per unit area in the channel induced by V_{GS}. Any variations of n_{ch} change Q_G and V_{GS}. From eq 3 we get:

$$\frac{dV_{GS}}{dQ_G} = \frac{1}{C_G} + \frac{dV_{ch}}{dQ_G} \quad (4)$$

which leads to

$$\Delta Q_G = (1/C_G + 1/C_Q)^{-1} \cdot \Delta V_{GS} \quad (5)$$

where C_Q = dQ_G/dV_{ch} is the SLG quantum capacitance[90,91] that characterizes the changes of the channel potential ΔV_{ch} as a result of additional gating ΔQ_G, and $(1/C_G + 1/C_Q)^{-1}$ is the total capacitance C_{tot}.

To calculate Q_G and Δn_{ch}, we first need to find C_G and C_Q. In PE gating, C_G is associated with the electric double layer (EDL) at the SLG/electrolyte interface.[53,90,92,93] The EDL acts like a parallel-plate capacitor with a dielectric layer thickness of the order of the Debye length λ_D, so that C_G = C_{EDL} = $\epsilon\epsilon_0/\lambda_D$, where ϵ is the PE dielectric constant, and ϵ_0 is the vacuum permittivity. In principle, for a monovalent electrolyte, λ_D can be explicitly calculated[94] if the electrolyte concentration is known. However, in the presence of a polymer matrix, the electrolyte ions can form complexes with polymer chains,[95] therefore the precise ion concentration is difficult to measure. For PE gating, different EDL thicknesses in the range ∼1−5 nm have been reported.[53,54,92,93] To estimate C_{EDL} in our devices,

DOI: 10.1021/acsnano.6b05109
ACS Nano 2016, 10, 8252−8262

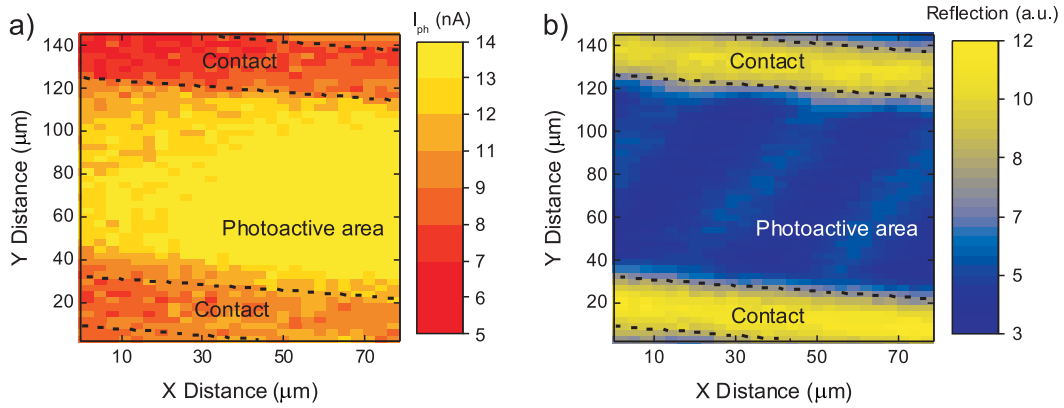

Figure 8. (a) Photocurrent map of channel area, simultaneously measured with backscattered light map. A uniform signal is observed in the channel area (between the electrodes). (b) Reflection map of backscattered light from the device channel. The yellow areas, corresponding to the contact areas, show higher reflectance than the substrate (in blue).

we take $\lambda_D \sim 2$ nm[53] and the dielectric constant of the poly(ethylene oxide) matrix to be $\epsilon \sim 5$,[96] as done in ref 53. As a result, we obtain $C_{EDL} = 2.2 \times 10^{-6}$ F/cm^2. This is the same order of magnitude as the SLG C_Q.[90] Therefore, the latter cannot be neglected in eq 5. C_Q is given by[90]

$$C_Q \approx \frac{2q^2}{\hbar v_F \sqrt{\pi}} \cdot \sqrt{n_{ch} + n_i} \tag{6}$$

where $\hbar$ is the reduced Planck constant, $v_F = 1.1 \times 10^6$ m/s is the SLG Fermi velocity,[80,97] and n_i is the intrinsic carrier concentration in SLG near the Dirac point induced by charge impurities, defects and local potential fluctuations in the SLG channel.[90,98−100] From our Raman and transconductance measurements we estimate $n_i \sim 3 \times 10^{12}$ cm^{-2}. From eq 6 we then get $C_Q = 4 \times 10^{-6}$ F/cm^2 at V_{CNP}. From Figure 6a, and extracting ΔV_{CNP} between the dark current and the transfer curves measured under illumination, and with eq 5, we get Δn_{ch} ranging from 4 to 8 $\times 10^{11}$ cm^{-2} for P_o going from 100 μW to 4 mW. As a result, we obtain $G_{PD} \sim 5 \times 10^4$ at $V_{DS} = 0.1$ V for different P_o as shown in Figure 9. As discussed previously, G_{PD} becomes larger for higher V_{DS}. Thus, we measure an increase of almost 1 order of magnitude ($G_{PD} \sim 4 \times 10^5$ at $P_o = 100$ μW) for V_{DS} going from 0.1 to 1 V.

Finally, we test I_{ph} as a function of bending using a Deben Microtest three-point bending setup (Figure 10a). In this case, $r_b = [h^2 + (L/2)^2]/2h$, where L is the chord of circumference connecting the two ends of the arc, and h is the height at the chord midpoint. The plotted values of I_{ph} in the bent state at each r_b ($I_{ph,bend}$) are normalized to the values of I_{ph} measured at rest with the sample in the flat position ($I_{ph,rest}$). Figure 10b plots the normalized $I_{ph,bend}/I_{ph,rest}$ for different r_b, showing

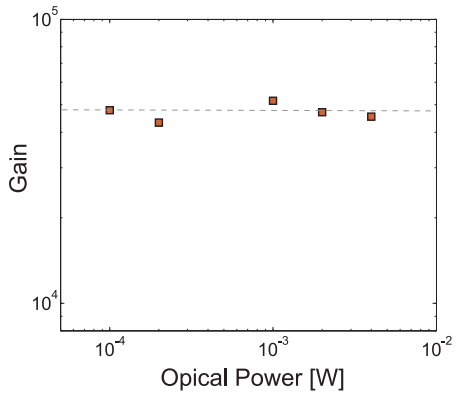

Figure 9. G_{PD} as a function of P_o at $V_{GS} = -1$ V and $V_{DS} = 0.1$ V.

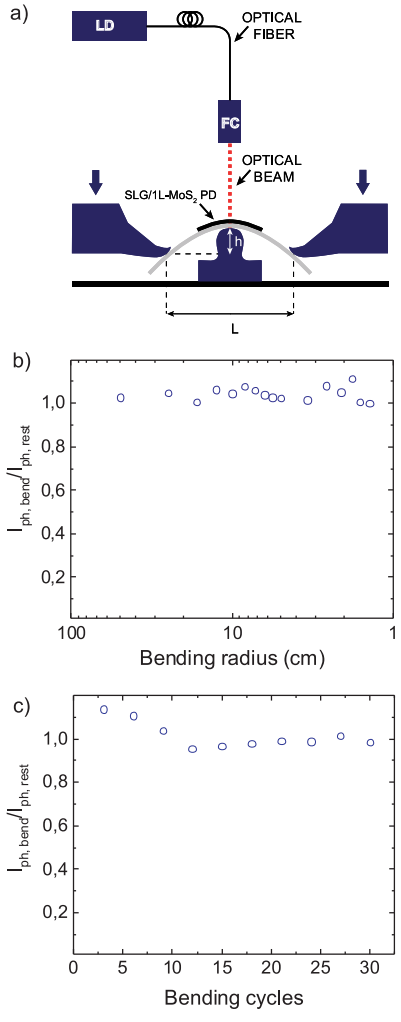

Figure 10. (a) Schematic three-point bending setup. LD = laser diode; FC= fiber collimator; (b) $I_{ph,bend}$ normalized to the value at rest $I_{ph,rest}$ as a function of r_b; (c) $I_{ph,bend}$ normalized to the value at rest $I_{ph,rest}$ as a function of the number of bending cycles.

DOI: 10.1021/acsnano.6b05109
ACS Nano 2016, 10, 8252−8262

deviations within 15% for r_b down to 1.4 cm. This r_b is comparable to that reported for semiconductor membrane PDs,[4,15] yet the latter have 2 orders of magnitude lower (<0.3 A/W) responsivities.[4,15] Although our r_b is five times larger than that reported for flexible single NW devices,[3,16−18] the area of our PDs (>40 mm^2) is at least 6 orders of magnitude larger than that of the NW devices (<5 μm^2). To test the device performance upon bending cycles, we first measure the photocurrent at rest ($I_{ph,rest}$, flat position) and then at the smallest r_b ($I_{ph,bend}$, r_b~1.4 cm), repeating these measurements for 30 bending cycles. Figure 10c plots $I_{ph,bend}/I_{ph,rest}$ as a function of bending cycles. This shows that our PDs retain stable photocurrent after multiple bending tests with a $I_{ph,bend}/I_{ph,rest}$ standard deviation ±12%.

CONCLUSIONS

We reported polymer electrolyte gated, flexible photodetectors, for visible wavelengths with external responsivity up to ~45.5 A/W, photoconductive gain ~4 × 10^5, operation voltage <1 V, and optical transparency >82%. The responsivity is at least 2 orders of magnitude higher than in semiconductor flexible membranes. The devices show stable performance upon bending for radii of curvature larger than ~1.4 cm. Owing to their responsivity, flexibility, transparency, and low operation voltage, our photodetectors can be attractive for wearable, biomedical, and low-power optoelectronic applications.[11,12,17]

METHODS

1L-MoS_2 is epitaxially grown by CVD on c-plane sapphire substrates.[61] These are annealed at 1000 °C in air for 1 h after consecutive cleaning by acetone/isopropyl alcohol/DI water. They are then placed face-down above a crucible containing ~5 mg MoO_3 (≥99.998% Alfa Aesar). This is loaded into a 32 mm outer diameter quartz tube placed in a split-tube three-zone furnace. A second crucible containing 350 mg sulfur (≥99.99% purity, Sigma-Aldrich) is located upstream from the growth substrates. Ultrahigh-purity Ar is used as carrier gas at atmospheric pressure. The procedure is to ramp the temperature to 300 °C with 200 sccm Ar flow, set to 300 °C for 10 min, ramp to 700 °C (50 °C/min increase temperature rate) with 10 sccm Ar flow, set at 700 °C for 10 min, cool to 570 °C with 10 sccm of Ar, increase the gas flow to 200 sccm and open the furnace for rapid cooling.[61] SLG is grown on a 35 μm Cu foil, following the process described in ref 51. The substrate is annealed in hydrogen atmosphere (H_2, 20 sccm) up to 1000 °C for 30 min. Then, 5 sccm CH_4 is added to initiate growth.[51,62] The sample is then cooled in vacuum (1 mTorr) to room temperature and removed from the chamber.

AUTHOR INFORMATION

Corresponding Author

*E-mail: acf26@eng.cam.ac.uk.

Author Contributions

§These authors contributed equally.

Notes

The authors declare no competing financial interest.

ACKNOWLEDGMENTS

We acknowledge funding from the EU Graphene Flagship, ERC Grant Hetero2D, EPSRC grant nos. EP/509 K01711X/1, EP/K017144/1, EP/N010345/1, EP/M507799/5101, and EP/L016087/1, Swiss SNF Sinergia Grant no. 147607, and Marie Curie ITN network MoWSeS (grant no. 317451).

REFERENCES

(1) Akinwande, D.; Petrone, N.; Hone, J. Two-Dimensional Flexible Nanoelectronics. *Nat. Commun.* **2014**, *5*, 5678.

(2) Ryhänen, T. *Nanotechnologies for Future Mobile Devices*; Cambridge University Press: Cambridge, U.K., 2010.

(3) Liu, Z.; Chen, G.; Liang, B.; Yu, G.; Huang, H.; Chen, D.; Shen, G. Fabrication of High-Quality ZnTe Nanowires Toward High-Performance Rigid/Flexible Visible-Light Photodetectors. *Opt. Express* **2013**, *21*, 7799−7810.

(4) Yuan, H.-C.; Shin, J.; Qin, G.; Sun, L.; Bhattacharya, P.; Lagally, M. G.; Celler, G. K.; Ma, Z. Flexible Photodetectors on Plastic Substrates by Use of Printing Transferred Single-Crystal Germanium Membranes. *Appl. Phys. Lett.* **2009**, *94*, 013102.

(5) Park, S.-I.; Xiong, Y.; Kim, R.-H.; Elvikis, P.; Meitl, M.; Kim, D.-H.; Wu, J.; Yoon, J.; Yu, C.-J.; Liu, Z.; Huang, Y.; Hwang, K.-C.; Ferreira, P.; Li, X.; Choquette, K.; Rogers, J. A. Printed Assemblies of Inorganic Light-Emitting Diodes for Deformable and Semitransparent Displays. *Science* **2009**, *325*, 977−981.

(6) Qiang, Z.; Yang, H.; Chen, L.; Pang, H.; Ma, Z.; Zhou, W. Fano Filters Based on Transferred Silicon Nanomembranes on Plastic Substrates. *Appl. Phys. Lett.* **2008**, *93*, 061106.

(7) Bosman, E.; Van Steenberge, G.; Van Hoe, B.; Missinne, J.; Vanfleteren, J.; Van Daele, P. Highly Reliable Flexible Active Optical Links. *IEEE Photonics Technol. Lett.* **2010**, *22*, 287−289.

(8) Chen, Z.; Ren, W.; Gao, L.; Liu, B.; Pei, S.; Cheng, H.-M. Three-Dimensional Flexible and Conductive Interconnected Graphene Networks Grown by Chemical Vapour Deposition. *Nat. Mater.* **2011**, *10*, 424−428.

(9) Shahi, S. Photovoltaics: Flexible Optoelectronics. *Nat. Photonics* **2010**, *4*, 506.

(10) Yoon, J.; Li, L.; Semichaevsky, A. V.; Ryu, J. H.; Johnson, H. T.; Nuzzo, R. G.; Rogers, J. A. Flexible Concentrator Photovoltaics Based on Microscale Silicon Solar Cells Embedded in Luminescent Waveguides. *Nat. Commun.* **2011**, *2*, 343.

(11) Kim, D.-H.; Lu, N.; Ma, R.; Kim, Y.-S.; Kim, R.-H.; Wang, S.; Wu, J.; Won, S. M.; Tao, H.; Islam, A.; Yu, K. J.; Kim, T.-I.; Chowdhury, R.; Ying, M.; Xu, L.; Li, M.; Chung, H.-J.; Keum, H.; McCormick, M.; Liu, P.; et al. Epidermal Electronics. *Science* **2011**, *333*, 838−843.

(12) Ko, H. C.; Stoykovich, M. P.; Song, J.; Malyarchuk, V.; Choi, W. M.; Yu, C.-J.; Geddes, J. B., III; Xiao, J.; Wang, S.; Huang, Y.; Rogers, J. A. A Hemispherical Electronic Eye Camera Based on Compressible Silicon Optoelectronics. *Nature* **2008**, *454*, 748−753.

(13) Blakemore, J. S. Semiconducting and Other Major Properties of Gallium-Arsenide. *J. Appl. Phys.* **1982**, *53*, 123−181.

(14) MacMillan, N. H. The Theoretical Strength of Solids. *J. Mater. Sci.* **1972**, *7*, 239−254.

(15) Yang, W.; Yang, H.; Qin, G.; Ma, Z.; Berggren, J.; Hammar, M.; Soref, R.; Zhou, W. Large-Area InP-Based Crystalline Nanomembrane Flexible Photodetectors. *Appl. Phys. Lett.* **2010**, *96*, 121107.

(16) Chen, G.; Liang, B.; Liu, Z.; Yu, G.; Xie, X.; Luo, T.; Xie, Z.; Chen, D.; Zhu, M.-Q.; Shen, G. High Performance Rigid and Flexible Visible-Light Photodetectors Based on Aligned X(In, Ga)P Nanowire Arrays. *J. Mater. Chem. C* **2014**, *2*, 1270−1277.

(17) Lee, S.; Jung, S. W.; Park, S.; Ahn, J.; Hong, S. J.; Yoo, H. J.; Lee, M. H.; Cho, D. I. Ultra-High Responsivity, Silicon Nanowire Photodetectors for Retinal Prosthesis. In *IEEE MEMS 25th International Conference*, Paris, France, January 29−February 2, 2012; IEEE: New York; pp 1364−1367.

(18) Yu, G.; Liu, Z.; Xie, X.; Ouyang, X.; Shen, G. Flexible Photodetectors with Single-Crystalline GaTe Nanowires. *J. Mater. Chem. C* **2014**, *2*, 6104−6110.

(19) Sze, S. M.; Kwok, K. N. *Physics of Semiconductor Devices*; Wiley: New York, 2006.

(20) Bonaccorso, F.; Sun, Z.; Hasan, T.; Ferrari, A. C. Graphene Photonics and Optoelectronics. *Nat. Photonics* **2010**, *4*, 611−622.

(21) Ferrari, A. C.; Bonaccorso, F.; Fal'ko, V.; Novoselov, K. S.; Roche, S.; Boggild, P.; Borini, S.; Koppens, F. H. L.; Palermo, V.; Pugno, N.; Garrido, J. A.; Sordan, R.; Bianco, A.; Ballerini, L.; Prato,

DOI: 10.1021/acsnano.6b05109
ACS Nano 2016, 10, 8252−8262

M.; Lidorikis, E.; Kivioja, J.; Marinelli, C.; Ryhänen, T.; Morpurgo, A.; et al. Science and Technology Roadmap for Graphene, Related Two-Dimensional Crystals, and Hybrid Systems. *Nanoscale* **2015**, *7*, 4598−4810.
(22) Koppens, F. H. L.; Mueller, T.; Avouris, P.; Ferrari, A. C.; Vitiello, M. S.; Polini, M. Photodetectors Based on Graphene, Other Two-Dimensional Materials and Hybrid Systems. *Nat. Nanotechnol.* **2014**, *9*, 780−793.
(23) Sun, Z. P.; Hasan, T.; Torrisi, F.; Popa, D.; Privitera, G.; Wang, F. Q.; Bonaccorso, F.; Basko, D. M.; Ferrari, A. C. Graphene Mode-Locked Ultrafast Laser. *ACS Nano* **2010**, *4*, 803−810.
(24) Kim, K. S.; Zhao, Y.; Jang, H.; Lee, S. Y.; Kim, J. M.; Kim, K. S.; Ahn, J.-H.; Kim, P.; Choi, J.-Y.; Hong, B. H. Large-Scale Pattern Growth of Graphene Films for Stretchable Transparent Electrodes. *Nature* **2009**, *457*, 706−710.
(25) Baugher, B. W. H.; Churchill, H. O. H.; Yang, Y.; Jarillo-Herrero, P. Optoelectronic Devices Based on Electrically Tunable p-n Diodes in a Monolayer Dichalcogenide. *Nat. Nanotechnol.* **2014**, *9*, 262−267.
(26) Pospischil, A.; Furchi, M. M.; Mueller, T. Solar-Energy Conversion and Light Emission in an Atomic Monolayer p-n Diode. *Nat. Nanotechnol.* **2014**, *9*, 257−261.
(27) Lopez-Sanchez, O.; Lembke, D.; Kayci, M.; Radenovic, A.; Kis, A. Ultrasensitive Photodetectors Based on Monolayer MoS_2. *Nat. Nanotechnol.* **2013**, *8*, 497−501.
(28) Xia, F. N.; Mueller, T.; Lin, Y. M.; Valdes-Garcia, A.; Avouris, P. Ultrafast Graphene Photodetector. *Nat. Nanotechnol.* **2009**, *4*, 839−843.
(29) Mueller, T.; Xia, F. N. A.; Avouris, P. Graphene Photodetectors for High-Speed Optical Communications. *Nat. Photonics* **2010**, *4*, 297−301.
(30) Liu, M.; Yin, X. B.; Ulin-Avila, E.; Geng, B. S.; Zentgraf, T.; Ju, L.; Wang, F.; Zhang, X. A Graphene-Based Broadband Optical Modulator. *Nature* **2011**, *474*, 64−67.
(31) Chen, J.; Badioli, M.; Alonso-Gonzalez, P.; Thongrattanasiri, S.; Huth, F.; Osmond, J.; Spasenovic, M.; Centeno, A.; Pesquera, A.; Godignon, P.; Zurutuza Elorza, A.; Camara, N.; de Abajo, F. J. G.; Hillenbrand, R.; Koppens, F. H. L. Optical Nano-Imaging of Gate-Tunable Graphene Plasmons. *Nature* **2012**, *487*, 77−81.
(32) Echtermeyer, T. J.; Britnell, L.; Jasnos, P. K.; Lombardo, A.; Gorbachev, R. V.; Grigorenko, A. N.; Geim, A. K.; Ferrari, A. C.; Novoselov, K. S. Strong Plasmonic Enhancement of Photovoltage in Graphene. *Nat. Commun.* **2011**, *2*, 458.
(33) Fei, Z.; Rodin, A. S.; Andreev, G. O.; Bao, W.; McLeod, A. S.; Wagner, M.; Zhang, L. M.; Zhao, Z.; Thiemens, M.; Dominguez, G.; Fogler, M. M.; Neto, A. H. C.; Lau, C. N.; Keilmann, F.; Basov, D. N. Gate-Tuning of Graphene Plasmons Revealed by Infrared Nano-Imaging. *Nature* **2012**, *487*, 82−85.
(34) Ju, L.; Geng, B.; Horng, J.; Girit, C.; Martin, M.; Hao, Z.; Bechtel, H. A.; Liang, X.; Zettl, A.; Shen, Y. R.; Wang, F. Graphene Plasmonics for Tunable Terahertz Metamaterials. *Nat. Nanotechnol.* **2011**, *6*, 630−634.
(35) Yan, H.; Li, X.; Chandra, B.; Tulevski, G.; Wu, Y.; Freitag, M.; Zhu, W.; Avouris, P.; Xia, F. Tunable Infrared Plasmonic Devices Using Graphene/Insulator Stacks. *Nat. Nanotechnol.* **2012**, *7*, 330−334.
(36) Furchi, M. M.; Pospischil, A.; Libisch, F.; Burgdörfer, J.; Mueller, T. Photovoltaic Effect in an Electrically Tunable Van der Waals Heterojunction. *Nano Lett.* **2014**, *14*, 4785−4791.
(37) Withers, F.; Del Pozo-Zamudio, O.; Mishchenko, A.; Rooney, A. P.; Gholinia, A.; Watanabe, K.; Taniguchi, T.; Haigh, S. J.; Geim, A. K.; Tartakovskii, A. I.; Novoselov, K. S. Light-Emitting Diodes by Band-Structure Engineering in Van der Waals Heterostructures. *Nat. Mater.* **2015**, *14*, 301−306.
(38) Hu, P. A.; Wang, L. F.; Yoon, M.; Zhang, J.; Feng, W.; Wang, X. N.; Wen, Z. Z.; Idrobo, J. C.; Miyamoto, Y.; Geohegan, D. B.; Xiao, K. Highly Responsive Ultrathin GaS Nanosheet Photodetectors on Rigid and Flexible Substrates. *Nano Lett.* **2013**, *13*, 1649−1654.
(39) Hsiao, Y.-J.; Fang, T.-H.; Ji, L.-W.; Yang, B.-Y. Red-Shift Effect and Sensitive Responsivity of MoS_2/ZnO Flexible Photodetectors. *Nanoscale Res. Lett.* **2015**, *10*, 443.
(40) Britnell, L.; Ribeiro, R. M.; Eckmann, A.; Jalil, R.; Belle, B. D.; Mishchenko, A.; Kim, Y. J.; Gorbachev, R. V.; Georgiou, T.; Morozov, S. V.; Grigorenko, A. N.; Geim, A. K.; Casiraghi, C.; Castro Neto, A. H.; Novoselov, K. S. Strong Light-Matter Interactions in Heterostructures of Atomically Thin Films. *Science* **2013**, *340*, 1311−1314.
(41) Tamalampudi, S. R.; Lu, Y. Y.; Kumar, U. R.; Sankar, R.; Liao, C. D.; Moorthy, B. K.; Cheng, C. H.; Chou, F. C.; Chen, Y. T. High Performance and Bendable Few-Layered InSe Photodetectors with Broad Spectral Response. *Nano Lett.* **2014**, *14*, 2800−2806.
(42) Amani, M.; Burke, R. A.; Proie, R. M.; Dubey, M. Flexible Integrated Circuits and Multifunctional Electronics Based on Single Atomic Layers of MoS_2 and Graphene. *Nanotechnology* **2015**, *26*, 115202.
(43) Xue, Y.; Zhang, Y.; Liu, Y.; Liu, H.; Song, J.; Sophia, J.; Liu, J.; Xu, Z.; Xu, Q.; Wang, Z.; Zheng, J.; Liu, Y.; Li, S.; Bao, Q. Scalable Production of a Few-Layer MoS_2/WS_2 Vertical Heterojunction Array and Its Application for Photodetectors. *ACS Nano* **2016**, *10*, 573−580.
(44) Finn, D. J.; Lotya, M.; Cunningham, G.; Smith, R. J.; McCloskey, D.; Donegan, J. F.; Coleman, J. N. Inkjet Deposition of Liquid-Exfoliated Graphene and MoS_2 Nanosheets for Printed Device Applications. *J. Mater. Chem. C* **2014**, *2*, 925−932.
(45) Withers, F.; Yang, H.; Britnell, L.; Rooney, A. P.; Lewis, E.; Felten, A.; Woods, C. R.; Romaguera, V. S.; Georgiou, T.; Eckmann, A.; Kim, Y. J.; Yeates, S. G.; Haigh, S. J.; Geim, A. K.; Novoselov, K. S.; Casiraghi, C. Heterostructures Produced from Nanosheet-Based Inks. *Nano Lett.* **2014**, *14*, 3987−3992.
(46) Liu, N.; Tian, H.; Schwartz, G.; Tok, J. B. H.; Ren, T.-L.; Bao, Z. Large-Area, Transparent, and Flexible Infrared Photodetector Fabricated Using p-n Junctions Formed by n-Doping Chemical Vapor Deposition Grown Graphene. *Nano Lett.* **2014**, *14*, 3702−3708.
(47) Velusamy, D. B.; Kim, R. H.; Cha, S.; Huh, J.; Khazaeinezhad, R.; Kassani, S. H.; Song, G.; Cho, S. M.; Cho, S. H.; Hwang, I.; Lee, J.; Oh, K.; Choi, H.; Park, C. Flexible Transition Metal Dichalcogenide Nanosheets for Band-Selective Photodetection. *Nat. Commun.* **2015**, *6*, 8063.
(48) Zhang, W. J.; Chuu, C. P.; Huang, J. K.; Chen, C. H.; Tsai, M. L.; Chang, Y. H.; Liang, C. T.; Chen, Y. Z.; Chueh, Y. L.; He, J. H.; Chou, M. Y.; Li, L. J. Ultrahigh-Gain Photodetectors Based on Atomically Thin Graphene-MoS_2 Heterostructures. *Sci. Rep.* **2014**, *4*, 3826.
(49) Faraj, M. G.; Ibrahim, K.; Ali, M. K. M. PET as a Plastic Substrate for the Flexible Optoelectronic Applications. *J. Optoelectron. Adv. Mater.* **2011**, *5*, 879−882.
(50) Martins, L. G. P.; Song, Y.; Zeng, T. Y.; Dresselhaus, M. S.; Kong, J.; Araujo, P. T. Direct Transfer of Graphene Onto Flexible Substrates. *Proc. Natl. Acad. Sci. U. S. A.* **2013**, *110*, 17762−17767.
(51) Bae, S.; Kim, H.; Lee, Y.; Xu, X.; Park, J. S.; Zheng, Y.; Balakrishnan, J.; Lei, T.; Kim, H. R.; Song, Y. I.; Kim, Y. J.; Kim, K. S.; Ozyilmaz, B.; Ahn, J. H.; Hong, B. H.; Iijima, S. Roll-to-Roll Production of 30-Inch Graphene Films for Transparent Electrodes. *Nat. Nanotechnol.* **2010**, *5*, 574−578.
(52) Thiele, C.; Das, R. *Carbon Nanotubes and Graphene for Electronics Applications 2010−2020*; IDTechEx: Boston, MA, 2010; p 98.
(53) Das, A.; Pisana, S.; Chakraborty, B.; Piscanec, S.; Saha, S. K.; Waghmare, U. V.; Novoselov, K. S.; Krishnamurthy, H. R.; Geim, A. K.; Ferrari, A. C.; Sood, A. K. Monitoring Dopants by Raman Scattering in an Electrochemically Top-Gated Graphene Transistor. *Nat. Nanotechnol.* **2008**, *3*, 210−215.
(54) Das, A.; Chakraborty, B.; Piscanec, S.; Pisana, S.; Sood, A. K.; Ferrari, A. C. Phonon Renormalization in Doped Bilayer Graphene. *Phys. Rev. B: Condens. Matter Mater. Phys.* **2009**, *79*, 155417.
(55) Sup Choi, M.; Lee, G.-H.; Yu, Y.-J.; Lee, D.-Y.; Hwan Lee, S.; Kim, P.; Hone, J.; Jong Yoo, W. Controlled Charge Trapping by Molybdenum Disulphide and Graphene in Ultrathin Heterostructured Memory Devices. *Nat. Commun.* **2013**, *4*, 1624.

DOI: 10.1021/acsnano.6b05109
ACS Nano 2016, 10, 8252−8262

(56) Das, S.; Chen, H.-Y.; Penumatcha, A. V.; Appenzeller, J. High Performance Multilayer MoS_2 Transistors with Scandium Contacts. *Nano Lett.* **2013**, *13*, 100−105.
(57) Shan, B.; Cho, K. First Principles Study of Work Functions of Single Wall Carbon Nanotubes. *Phys. Rev. Lett.* **2005**, *94*, 236602.
(58) Yu, Y.-J.; Zhao, Y.; Ryu, S.; Brus, L. E.; Kim, K. S.; Kim, P. Tuning the Graphene Work Function by Electric Field Effect. *Nano Lett.* **2009**, *9*, 3430−3434.
(59) Kim, B. J.; Jang, H.; Lee, S.-K.; Hong, B. H.; Ahn, J.-H.; Cho, J. H. High-Performance Flexible Graphene Field Effect Transistors with Ion Gel Gate Dielectrics. *Nano Lett.* **2010**, *10*, 3464−3466.
(60) Lee, S. K.; Jang, H. Y.; Jang, S.; Choi, E.; Hong, B. H.; Lee, J.; Park, S.; Ahn, J. H. All Graphene-Based Thin Film Transistors on Flexible Plastic Substrates. *Nano Lett.* **2012**, *12*, 3472−3476.
(61) Dumcenco, D.; Ovchinnikov, D.; Marinov, K.; Lazić, P.; Gibertini, M.; Marzari, N.; Sanchez, O. L.; Kung, Y.-C.; Krasnozhon, D.; Chen, M.-W.; Bertolazzi, S.; Gillet, P. Large-Area Epitaxial Monolayer MoS_2. *ACS Nano* **2015**, *9*, 4611−4620.
(62) Li, X. S.; Cai, W. W.; An, J. H.; Kim, S.; Nah, J.; Yang, D. X.; Piner, R.; Velamakanni, A.; Jung, I.; Tutuc, E.; Banerjee, S. K.; Colombo, L.; Ruoff, R. S. Large-Area Synthesis of High-Quality and Uniform Graphene Films on Copper Foils. *Science* **2009**, *324*, 1312−1314.
(63) Verble, J. L.; Wieting, T. J. Lattice Mode Degeneracy in MoS_2 and Other Layer Compounds. *Phys. Rev. Lett.* **1970**, *25*, 362−365.
(64) Wieting, T. J.; Verble, J. L. Infrared and Raman Studies of Long-Wavelength Optical Phonons in Hexagonal MoS_2. *Phys. Rev. B* **1971**, *3*, 4286−4292.
(65) Lee, C.; Yan, H. G.; Brus, L. E.; Heinz, T. F.; Hone, J.; Ryu, S. Anomalous Lattice Vibrations of Single- and Few-Layer MoS_2. *ACS Nano* **2010**, *4*, 2695−2700.
(66) Li, H.; Zhang, Q.; Yap, C. C. R.; Tay, B. K.; Edwin, T. H. T.; Olivier, A.; Baillargeat, D. From Bulk to Monolayer MoS_2: Evolution of Raman Scattering. *Adv. Funct. Mater.* **2012**, *22*, 1385−1390.
(67) Porto, S. P. S.; Krishnan, R. S. Raman Effect of Corundum. *J. Chem. Phys.* **1967**, *47*, 1009−1012.
(68) Lagatsky, A. A.; Sun, Z.; Kulmala, T. S.; Sundaram, R. S.; Milana, S.; Torrisi, F.; Antipov, O. L.; Lee, Y.; Ahn, J. H.; Brown, C. T. A.; Sibbett, W.; Ferrari, A. C. 2μm Solid-State Laser Mode-Locked by Single-Layer Graphene. *Appl. Phys. Lett.* **2013**, *102*, 013113.
(69) Ferrari, A. C.; Basko, D. M. Raman Spectroscopy as a Versatile Tool for Studying the Properties of Graphene. *Nat. Nanotechnol.* **2013**, *8*, 235−246.
(70) Ferrari, A. C.; Meyer, J. C.; Scardaci, V.; Casiraghi, C.; Lazzeri, M.; Mauri, F.; Piscanec, S.; Jiang, D.; Novoselov, K. S.; Roth, S.; Geim, A. K. Raman Spectrum of Graphene and Graphene Layers. *Phys. Rev. Lett.* **2006**, *97*, 187401.
(71) Cancado, L. G.; Jorio, A.; Ferreira, E. H.; Stavale, F.; Achete, C. A.; Capaz, R. B.; Moutinho, M. V.; Lombardo, A.; Kulmala, T. S.; Ferrari, A. C. Quantifying Defects in Graphene *Via* Raman Spectroscopy at Different Excitation Energies. *Nano Lett.* **2011**, *11*, 3190−3196.
(72) Ferrari, A. C.; Robertson, J. Interpretation of Raman Spectra of Disordered and Amorphous Carbon. *Phys. Rev. B: Condens. Matter Mater. Phys.* **2000**, *61*, 14095−14107.
(73) Basko, D. M.; Piscanec, S.; Ferrari, A. C. Electron-Electron Interactions and Doping Dependence of the Two-Phonon Raman Intensity in Graphene. *Phys. Rev. B: Condens. Matter Mater. Phys.* **2009**, *80*, 165413.
(74) Bruna, M.; Ott, A. K.; Ijas, M.; Yoon, D.; Sassi, U.; Ferrari, A. C. Doping Dependence of the Raman Spectrum of Defected Graphene. *ACS Nano* **2014**, *8*, 7432−7441.
(75) Mak, K. F.; Lee, C.; Hone, J.; Shan, J.; Heinz, T. F. Atomically Thin MoS_2: a New Direct-Gap Semiconductor. *Phys. Rev. Lett.* **2010**, *105*, 136805.
(76) Bonaccorso, F.; Lombardo, A.; Hasan, T.; Sun, Z. P.; Colombo, L.; Ferrari, A. C. Production and Processing of Graphene and 2d Crystals. *Mater. Today* **2012**, *15*, 564−589.
(77) Boerio, F. J.; Bahl, S. K.; McGraw, G. E. Vibrational Analysis of Polyethylene Terephthalate and Its Deuterated Derivatives. *J. Polym. Sci., Polym. Phys. Ed.* **1976**, *14*, 1029−1046.
(78) Qiu, D. Y.; da Jornada, F. H.; Louie, S. G. Optical Spectrum of MoS_2: Many-Body Effects and Diversity of Exciton States. *Phys. Rev. Lett.* **2013**, *111*, 216805.
(79) Nair, R. R.; Blake, P.; Grigorenko, A. N.; Novoselov, K. S.; Booth, T. J.; Stauber, T.; Peres, N. M. R.; Geim, A. K. Fine Structure Constant Defines Visual Transparency of Graphene. *Science* **2008**, *320*, 1308.
(80) Novoselov, K. S.; Geim, A. K.; Morozov, S. V.; Jiang, D.; Katsnelson, M. I.; Grigorieva, I. V.; Dubonos, S. V.; Firsov, A. A. Two-Dimensional Gas of Massless Dirac Fermions in Graphene. *Nature* **2005**, *438*, 197−200.
(81) Lemme, M. C.; Echtermeyer, T. J.; Baus, M.; Kurz, H. A Graphene Field-Effect Device. *IEEE Electron Device Lett.* **2007**, *28*, 282−284.
(82) Wehling, T. O.; Novoselov, K. S.; Morozov, S. V.; Vdovin, E. E.; Katsnelson, M. I.; Geim, A. K.; Lichtenstein, A. I. Molecular Doping of Graphene. *Nano Lett.* **2008**, *8*, 173−177.
(83) Ye, J. T.; Craciun, M. F.; Koshino, M.; Russo, S.; Inoue, S.; Yuan, H. T.; Shimotani, H.; Morpurgo, A. F.; Iwasa, Y. Accessing the Transport Properties of Graphene and its Multilayers at High Carrier Density. *Proc. Natl. Acad. Sci. U. S. A.* **2011**, *108*, 13002−13006.
(84) Sirringhaus, H.; Kawase, T.; Friend, R. H.; Shimoda, T.; Inbasekaran, M.; Wu, W.; Woo, E. P. High-Resolution Inkjet Printing of All-Polymer Transistor Circuits. *Science* **2000**, *290*, 2123−2126.
(85) Azaïs, P.; Duclaux, L.; Florian, P.; Massiot, D.; Lillo-Rodenas, M.-A.; Linares-Solano, A.; Peres, J.-P.; Jehoulet, C.; Beguin, F. Causes of Supercapacitors Ageing in Organic Electrolyte. *J. Power Sources* **2007**, *171*, 1046−1053.
(86) Efetov, D. K.; Kim, P. Controlling Electron-Phonon Interactions in Graphene at Ultrahigh Carrier Densities. *Phys. Rev. Lett.* **2010**, *105*, 256805.
(87) Konstantatos, G.; Badioli, M.; Gaudreau, L.; Osmond, J.; Bernechea, M.; Garcia de Arquer, F. P.; Gatti, F.; Koppens, F. H. Hybrid Graphene-Quantum Dot Phototransistors with Ultrahigh Gain. *Nat. Nanotechnol.* **2012**, *7*, 363−368.
(88) Meric, I.; Han, M. Y.; Young, A. F.; Ozyilmaz, B.; Kim, P.; Shepard, K. L. Current Saturation in Zero-Bandgap, Top-Gated Graphene Field-Effect Transistors. *Nat. Nanotechnol.* **2008**, *3*, 654−659.
(89) Robinson, J. A.; LaBella, M.; Zhu, M.; Hollander, M.; Kasarda, R.; Hughes, Z.; Trumbull, K.; Cavalero, R.; Snyder, D. Contacting Graphene. *Appl. Phys. Lett.* **2011**, *98*, 053103.
(90) Xia, J.; Chen, F.; Li, J.; Tao, N. Measurement of the Quantum Capacitance of Graphene. *Nat. Nanotechnol.* **2009**, *4*, 505−509.
(91) Fang, T.; Konar, A.; Xing, H.; Jena, D. Carrier Statistics and Quantum Capacitance of Graphene Sheets and Ribbons. *Appl. Phys. Lett.* **2007**, *91*, 092109.
(92) Ozel, T.; Gaur, A.; Rogers, J. A.; Shim, M. Polymer Electrolyte Gating of Carbon Nanotube Network Transistors. *Nano Lett.* **2005**, *5*, 905−911.
(93) Lu, C.; Fu, Q.; Huang, S.; Liu, J. Polymer Electrolyte-Gated Carbon Nanotube Field-Effect Transistor. *Nano Lett.* **2004**, *4*, 623−627.
(94) Russel, W. B.; Saville, D. A.; Schowalter, W. R. *Colloidal Dispersions*; Cambridge University Press: Cambridge, U.K., 1989.
(95) Salomon, M.; Xu, M.; Eyring, E. M.; Petrucci, S. Molecular Structure and Dynamics of $LiClO_4$-Polyethylene Oxide-400 (Dimethyl Ether and Diglycol Systems) at 25°C. *J. Phys. Chem.* **1994**, *98*, 8234−8244.
(96) Boyd, R. H. The Dielectric Constant of Lamellar Semicrystalline Polymers. *J. Polym. Sci., Polym. Phys. Ed.* **1983**, *21*, 505−514.
(97) Zhang, Y. B.; Tan, Y. W.; Stormer, H. L.; Kim, P. Experimental Observation of the Quantum Hall Effect and Berry's Phase in Graphene. *Nature* **2005**, *438*, 201−204.

DOI: 10.1021/acsnano.6b05109
ACS Nano 2016, 10, 8252−8262

(98) Adam, S.; Hwang, E. H.; Galitski, V. M.; Das Sarma, S. A Self-Consistent Theory for Graphene Transport. *Proc. Natl. Acad. Sci. U. S. A.* **2007**, *104*, 18392−18397.
(99) Chen, J. H.; Jang, C.; Adam, S.; Fuhrer, M. S.; Williams, E. D.; Ishigami, M. Charged-Impurity Scattering in Graphene. *Nat. Phys.* **2008**, *4*, 377−381.
(100) Galitski, V. M.; Adam, S.; Das Sarma, S. Statistics of Random Voltage Fluctuations and the Low-Density Residual Conductivity of Graphene. *Phys. Rev. B: Condens. Matter Mater. Phys.* **2007**, *76*, 245405.

DOI: 10.1021/acsnano.6b05109
ACS Nano 2016, 10, 8252−8262